

# Fe, P Heteronuclear Catalytic Pairs with Hydrogen Bonding Regulated the Oxygen Reduction Reaction Kinetics for an Ultrastable Oxygen Depolarized Cathode

Fenghong Lu, Yuanyuan Zhang, Lingbo Zong\*, Chengbin Wang, Kaicai Fan, Cheng-Hao Chuang, Porun Liu, Zumin Wang\*, Lei Wang\*, and Bin Li\*



Cite This: *ACS Nano* 2025, 19, 40128–40139



Read Online

ACCESS |

Metrics & More

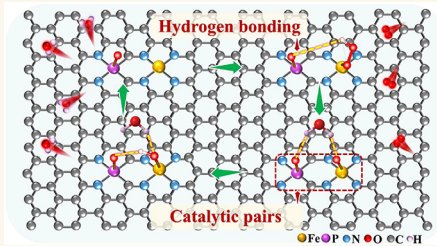


Article Recommendations



Supporting Information

**ABSTRACT:** The rational design of efficient oxygen reduction reaction (ORR) catalysts with maximized atom utilization is essential for advancing the oxygen depolarized cathode technology. Here, we report atomically dispersed Fe, P heteronuclear catalytic pairs on hierarchical porous carbon, in which the hydrogen bond between Fe, P catalytic pairs and ORR intermediates significantly enhances the adsorption/desorption kinetics and lowers the rate-determining step barrier of OH\* desorption. Thus, Fe,P/HPC delivers an alkaline ORR performance with a half-wave potential ( $E_{1/2}$ ) of 0.92 V and retains ~90% of the initial activity even after 150 h operation. In addition, Fe,P/HPC achieves an  $E_{1/2}$  of 0.74 V in 0.1 M  $\text{HClO}_4$ . The Fe,P/HPC-based aqueous Zn-air battery (A-ZAB) achieves a high power density of  $262 \text{ mW cm}^{-2}$  and exhibits enhanced stability, sustaining a minimal voltage gap over 2800 h of constant-current cycling. Moreover, the quasi-solid-state Zn-air battery (QSS-ZAB) delivers a large open-circuit voltage of 1.52 V, while maintaining a cycling stability for over 95 h at 0.5, 1, and 2  $\text{mA cm}^{-2}$ , respectively. In the chlor-alkali process, the Fe,P/HPC||RuO<sub>2</sub> electrolyzer enables a large current density of  $300 \text{ mA cm}^{-2}$  at 1.66 V and maintains stability over 110 h. The present work pioneers the designing and construction of atomic-level heteronuclear catalysts for practical and durable cathode.



**KEYWORDS:** heteronuclear catalytic pairs, hierarchical porous structure, hydrogen bonding, oxygen reduction reaction, Zn–air battery, chlor-alkali electrolyzer

## INTRODUCTION

The development of renewable energy storage and conversion technologies (e.g., metal–air batteries and fuel cells) will minimize the dependence on fossil fuels and achieve net-zero emissions.<sup>1–3</sup> Meanwhile, adopting more advanced chemical processes can also significantly improve the energy utilization efficiency and reduce energy consumption.<sup>4</sup> For example, the oxygen depolarized cathode (ODC) technology, which replaces the hydrogen evolution reaction (HER) with the oxygen reduction reaction (ORR), can significantly lower the cathode potential, reducing over 30% electricity in the chlor-alkali industry.<sup>5,6</sup> However, the sluggish kinetics of the cathodic ORR in these applications severely constrain their commercialization.<sup>7,8</sup> This limitation has spurred the advancement of Pt-free ORR electrocatalysts with high performance, low cost, and enhanced durability.

Recently, transition metal single-atom catalysts (SACs) with a TM-N<sub>x</sub>/C configuration (TM = Fe, Co, Ni, Mn, etc.) have

been widely used as ideal alternatives to precious metal ORR catalysts, which offer maximum atom utilization, high intrinsic activity, and low cost.<sup>8,9</sup> Nevertheless, ORR kinetics are constrained by scaling relations, where the adsorption free energy of OOH\* is intrinsically linked to that of OH\*, with a nearly constant energy difference exceeding the optimal value.<sup>10</sup> Nonetheless, SACs can only rely on one kind of active site to activate all intermediates, which falls short in effectively handling multiple ORR intermediates (OOH\*, O\*, and OH\*) simultaneously.<sup>11</sup> This limitation restricts both the reaction rate and selectivity.<sup>12</sup> In contrast, catalysts with two or

Received: September 12, 2025

Revised: November 1, 2025

Accepted: November 4, 2025

Published: November 11, 2025



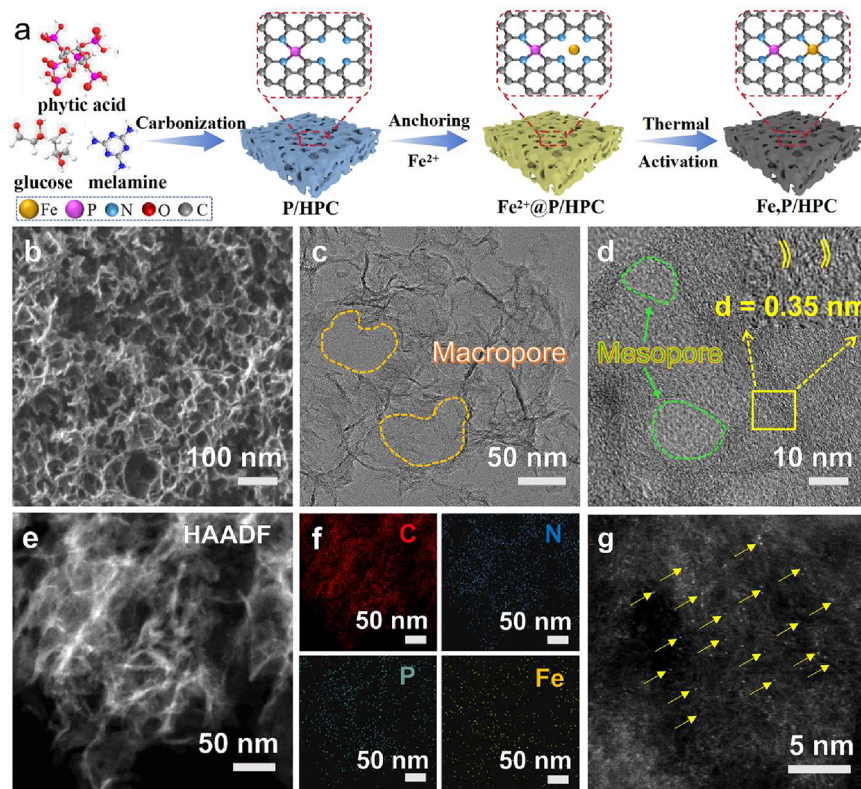


**Figure 1.** Synthesis scheme and morphology characterization of Fe<sub>3</sub>P/HPC. (a) Schematic illustration of the preparation of Fe<sub>3</sub>P/HPC. (b) SEM, (c) TEM, and (d) HRTEM images of Fe<sub>3</sub>P/HPC. (e, f) HAADF-STEM and the corresponding EDS mapping images of Fe<sub>3</sub>P/HPC. (g) AC HAADF-STEM image of Fe<sub>3</sub>P/HPC.

more adjacent atomic sites with complementary functionalities and synergistic effects can manage concurrent ORR intermediates through differential binding energies at distinct active sites.<sup>13,14</sup> This approach further enables the optimization of the ORR pathway through precise spatial modulation of the distance and arrangement of the active sites.<sup>15</sup>

As an extension of SACs, dual-atom catalysts (DACs) possess a distinctive structure of two kinds of atom sites, which have been reported to perform well for CO<sub>2</sub> reduction, N<sub>2</sub> fixation, and ORR because of synergistic effects, distance enhancement effects, and electronic modulation effects.<sup>16–18</sup> DACs introduce an additional degree of freedom for regulating the adsorption of intermediate species, thereby expanding the range of feasible adsorption configurations.<sup>11</sup> Critically, the interaction between two active sites can effectively modulate the activation energies and adsorption strengths of reaction intermediates, offering greater potential for designing and optimizing catalytic reactions.<sup>19,20</sup>

However, the majority of the current reports on DACs have concentrated on homonuclear or heteronuclear bimetallic pairs.<sup>21,22</sup> In many reported DACs, the prevailing view is that the catalytically active site resides at a single metal center with the second atom serving primarily to modulate its electronic structure.<sup>23</sup> In contrast, the potential of introducing a nonmetallic atom as a secondary active site has been largely overlooked. The ignorance of the catalytic role of nonmetallic sites has constrained both catalyst design versatility and a mechanistic understanding. To address this gap, the concept of a metal–nonmetal catalytic pair was recently introduced, wherein two adjacent but nonbonded atoms act cooperatively during catalysis.<sup>24–26</sup> Notably, nonmetal atoms have totally

different characteristics, bringing many more possibilities in tuning the active sites.<sup>27–29</sup> Recent studies have collectively underscored the critical role of nonmetal coordination in modulating the activity. For example, Zhai and co-workers achieved the introduction of nonmetal sulfur atoms into the coordination shell of Fe-NC, which lowered the spin state of the Fe center, facilitated the OH\* desorption of intermediates, and boosted the ORR performance.<sup>30</sup> Similarly, Cao et al. significantly reduced the ORR overpotential by incorporating the less electronegative boron atoms into the first coordination shell of the Fe site.<sup>31</sup> While current heteronuclear metal–nonmetal pairs such as Fe–S and Fe–B have shown promise in modulating the electronic structure of the metal center for enhanced ORR, their functionality is often confined to electronic effects. In contrast, phosphorus offers a strong oxygen affinity, readily adsorbing active OH\* and facilitating O=O bond cleavage to enhance activation and conversion.<sup>32</sup> The unique potential to form hydrogen bonds with reaction intermediates enables a P site in proximity to a Fe center not only to tune its electronic structure but also to directly participate in stabilizing transition states, offering a pathway to break the scaling relations. Specifically, hydrogen bonding between OOH\* (bound to Fe) and O (bound to P) stabilizes transition states, forming the basis of a hydrogen-bond-promoted ORR mechanism.<sup>33,34</sup> This interaction facilitates the protonation of OOH\*-Fe and expands OH\* coverage, forming the basis of a hydrogen-bond-promoted ORR mechanism.<sup>35,36</sup> Unfortunately, typical synthesis methods usually lead to random atom combinations and mixed active sites, posing significant challenges in controlling the distances, electronic interactions, and coordination modes for the metal–

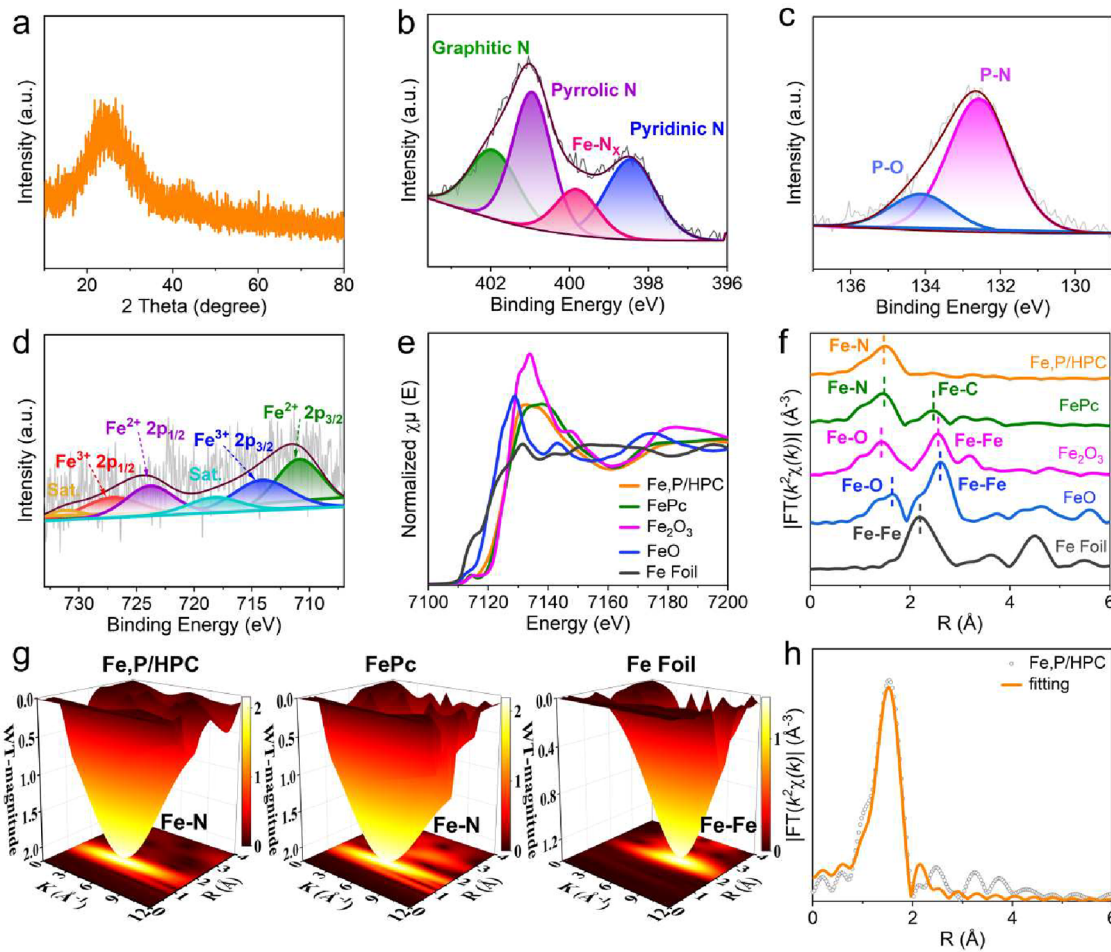


**Figure 2.** (a) XRD pattern of Fe<sub>3</sub>P/HPC. High-resolution (b) N 1s, (c) P 2p, and (d) Fe 2p XPS spectra of Fe<sub>3</sub>P/HPC. (e) Fe K-edge XANES spectra. (f) Fourier transform Fe K-edge EXAFS spectra of Fe<sub>3</sub>P/HPC, FePc, Fe<sub>2</sub>O<sub>3</sub>, FeO, and Fe foil. (g) Wavelet transform signals of  $k^2$ -weighted  $\chi(k)$  of Fe<sub>3</sub>P/HPC, FePc, and Fe foil. (h) Least squares fittings of FT-EXAFS spectra of Fe<sub>3</sub>P/HPC at R-space.

nonmetal catalytic pairs. There is still a long way to discover a universal principle for the rational design and precise preparation of metal–nonmetal catalytic pairs toward ORR and other desired reactions.

In this study, we successfully synthesized Fe and P heteronuclear catalytic pairs on hierarchical porous carbon (Fe<sub>3</sub>P/HPC) through an approach integrating the adsorption of transition metal complexes and thermal activation. The synergistic effect of adjacent Fe and P heteronuclear catalytic pairs, combined with abundant pores in carbon support, endows Fe<sub>3</sub>P/HPC with ORR activity and enhanced stability. Density functional theory (DFT) calculations further reveal that the hydrogen-bond interactions between the Fe and P heteronuclear catalytic pairs can effectively facilitate the adsorption/desorption of oxygen intermediates and lower the barrier of OH\* desorption during the catalytic process, thereby accelerating the ORR kinetics. Consequently, the as-prepared Fe<sub>3</sub>P/HPC achieves a half-wave potential ( $E_{1/2}$ ) of 0.92 V in 0.1 M KOH. When employed as the air cathode in an aqueous Zn–air battery (A-ZAB), Fe<sub>3</sub>P/HPC delivers a high peak power density of 262 mW cm<sup>-2</sup> and demonstrates long-term stability, sustaining a low charge–discharge voltage gap for over 2800 h at 10 mA cm<sup>-2</sup>. Notably, the Fe<sub>3</sub>P/HPC-based quasi-solid-state Zn–air battery (QSS-ZAB) attains an open-circuit voltage (OCV) of 1.52 V and a peak power density of 229 mW cm<sup>-2</sup>, while maintaining stable charge–discharge

cycling for 95 h with minimal voltage gaps at current densities of 0.5, 1.0, and 2.0 mA cm<sup>-2</sup>, respectively. Significantly, the Fe<sub>3</sub>P/HPC||RuO<sub>2</sub> chlor-alkali electrolyzer system achieves a large current density of 300 mA cm<sup>-2</sup> at 1.66 V, substantially lower than that of its Pt/C||RuO<sub>2</sub>-based counterpart. This work demonstrates that synergistic interactions in metal–nonmetal catalytic pairs provide a strategy for designing practical, efficient, and durable cathode catalysts.

## RESULTS AND DISCUSSION

**Synthesis and Structural Characterization.** The strategy for the synthesis of Fe<sub>3</sub>P/HPC is outlined in Figure 1a. First, the aerogel containing glucose, melamine, and phytic acid was thermally activated to obtain N, P-codoped in hierarchical porous carbon (P/HPC). Scanning electron microscopy (SEM) and transmission electron microscopy (TEM) images reveal that P/HPC exhibits a 3D porous structure (Figure S1). Subsequently, using iron acetate as the iron source and 1,10-phenanthroline as the ligand, Fe ions were captured and anchored within the P/HPC to form Fe<sup>2+</sup>@P/HPC. A subsequent thermal activation in a N<sub>2</sub> atmosphere results in Fe<sub>3</sub>P/HPC.

SEM and TEM (Figure 1b,c) images reveal that Fe<sub>3</sub>P/HPC exhibits a 3D porous morphology with a honeycomb-like network containing abundant interconnected macropores. Furthermore, the high-resolution TEM (HRTEM) image

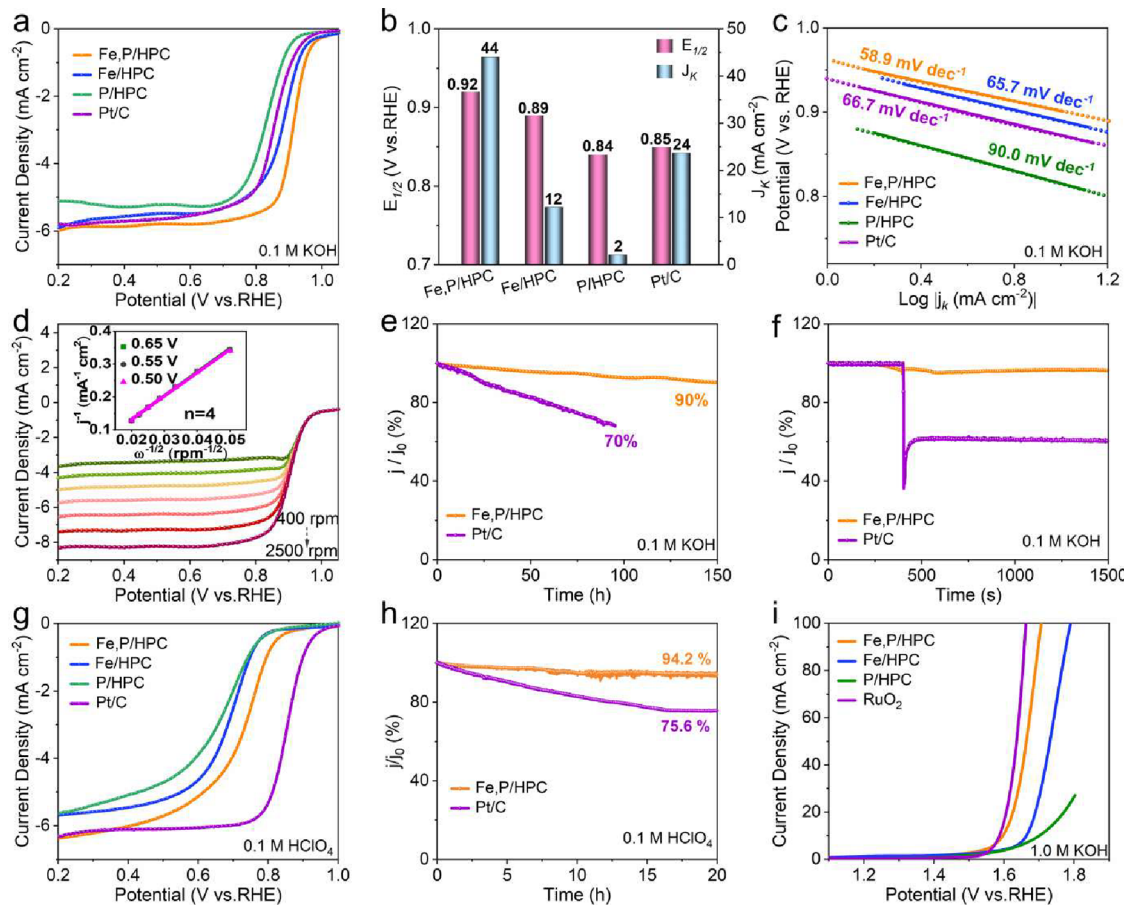


**Figure 3.** (a) ORR polarization curves. (b)  $E_{1/2}$  and  $J_k$  of Fe,P/HPC, Fe/HPC, P/HPC, and Pt/C. (c) Tafel plots of Fe,P/HPC, P/HPC, and Pt/C. (d) LSV curves of Fe,P/HPC recorded at different rotation speeds recorded in O<sub>2</sub>-saturated 0.1 M KOH. Inset: the corresponding K–L plots obtained from the corresponding LSV curves. (e) Chronoamperometric responses of Fe,P/HPC and Pt/C. (f) Methanol tolerance of Fe,P/HPC and Pt/C. (g) ORR polarization curves of Fe,P/HPC, Fe/HPC, P/HPC, and Pt/C in 0.1 M HClO<sub>4</sub>. (h) Chronoamperometric response of Fe,P/HPC and Pt/C in 0.1 M HClO<sub>4</sub>. (i) OER polarization curves of Fe,P/HPC, Fe/HPC, P/HPC, and RuO<sub>2</sub> in O<sub>2</sub>-saturated 1.0 M KOH at a scan rate of 5 mV s<sup>-1</sup>.

further shows well-defined mesoporous structures in Fe,P/HPC, with no evidence of Fe nanoparticles, as noted in Figure 1d. A closer inspection of Fe,P/HPC shows a distinguished interlayer spacing of 0.35 nm, corresponding to the (002) crystal planes of graphitic carbon.<sup>37</sup> The high-angle annular dark-field scanning transmission electron microscopy (HAADF-STEM) and corresponding energy-dispersive X-ray spectroscopy (EDS) mapping images show that C, N, P, and Fe elements are uniformly distributed throughout Fe,P/HPC (Figure 1e,f). The aberration-corrected HAADF-STEM (AC HAADF-STEM, Figure 1g) image of Fe,P/HPC identifies isolated bright dots, directly confirming the atomic-level dispersion of Fe species in hierarchical porous carbon. The content of Fe in Fe,P/HPC quantified via inductively coupled plasma optical emission spectrometry (ICP-OES) is 0.47 wt %.

The powder X-ray diffraction (XRD, Figure 2a) pattern of Fe,P/HPC exhibits two broad diffraction peaks located at around 26 and 44°, which are attributed to the (002) and (101) planes of the graphitic carbon.<sup>38</sup> The Raman spectra of Fe,P/HPC and P/HPC both exhibit two well-defined characteristic peaks of the D-band at ~1347 cm<sup>-1</sup> and the G-band at ~1600 cm<sup>-1</sup> (Figure S2). Apparently, the calculated  $I_D/I_G$  values are 1.05 for Fe,P/HPC and 1.03 for P/HPC, which indicates that both materials possess a high defect density. More importantly, these closely matched values

suggest that Fe doping has a negligible impact on the graphitization degree of the carbon support. The N<sub>2</sub> adsorption/desorption isotherm of Fe,P/HPC exhibits a type IV isotherm at relatively high pressures with a well-defined adsorption–desorption hysteresis return (H4 hysteresis return, Figure S3), verifying the micropores/mesoporous structure. Fe,P/HPC has a large Brunauer–Emmett–Teller (BET) surface area of 627 m<sup>2</sup> g<sup>-1</sup>, and the pore size distribution is primarily concentrated in the micropores and mesoporous range of 0.7–1.6 and 2.7–13.1 nm, respectively (Figure S4). The hierarchical porous structure of Fe,P/HPC ensures the accessibility of single-atom active sites and accelerates the mass transfer, contributing to the ORR performance.<sup>39</sup>

X-ray photoelectron spectroscopy (XPS) survey spectrum confirms the presence of Fe, C, N, and P elements in the carbon support (Figure S5). The high-resolution C 1s spectrum of Fe,P/HPC is deconvoluted into five peaks at binding energies of 284.8 eV (C–C), 285.6 eV (C–P), 286.6 eV (C–N), 288.0 eV (C=C), and 290.7 eV (O=C=O), respectively (Figure S6).<sup>40</sup> As shown in Figure 2b, the high-resolution N 1s spectrum can be deconvoluted into four individual peaks, assigned to pyridinic N (398.4 eV), Fe–N<sub>x</sub> (399.5 eV), pyrrolic N (400.9 eV), and graphitic N (401.7 eV), respectively.<sup>41</sup> Moreover, the high-resolution P 2p XPS spectrum exhibits two characteristic peaks at 134.1 eV (P–

O) and 132.5 eV (P–N), respectively (Figure 2c).<sup>32</sup> The presence of the P–O bond may arise from the surface oxidation due to the air exposure. The high-resolution Fe 2p spectrum is fitted with six peaks, assigned to Fe 2p<sub>3/2</sub> (Fe<sup>2+</sup> at 710.8 eV and Fe<sup>3+</sup> at 714.0 eV), Fe 2p<sub>1/2</sub> (Fe<sup>2+</sup> at 723.9 eV and Fe<sup>3+</sup> at 727.1 eV), and two satellite peaks (718.2 and 731.3 eV, Figure 2d).<sup>42</sup> The absence of apparent Fe<sup>0</sup> peaks indicates that Fe exists in the form of a single atom.

The chemical states and local coordination structures of Fe atoms in Fe<sub>x</sub>P/HPC were further systematically investigated by X-ray absorption spectroscopy (XAS). The Fe K-edge X-ray absorption near edge structure (XANES) spectrum in Figure 2e displays that the absorption edge of Fe<sub>x</sub>P/HPC is located close to FePc, suggesting that the oxidation state of Fe is +2.<sup>43</sup> The Fourier transform of the  $k^2$ -weighted extended X-ray absorption fine structure (FT-EXAFS, Figure 2f) spectrum shows that the R-space of Fe<sub>x</sub>P/HPC has only one main peak at  $\sim 1.50 \text{ \AA}$ , which is attributed to the Fe–N scattering path (similar to FePc).<sup>44</sup> There is no Fe–Fe bonding peak at  $2.20 \text{ \AA}$ , suggesting atomic dispersion of Fe in the Fe<sub>x</sub>P/HPC. Moreover, wavelet transform EXAFS (WT-EXAFS) analysis shows the maximum intensity at  $\sim 4.3 \text{ \AA}^{-1}$  in k-space, corresponding to the Fe–N coordination in Fe<sub>x</sub>P/HPC, which matches well with the FePc reference model (Figure 2g). The coordination number of Fe–N and the corresponding bond length are determined to be  $\sim 5.44$  and  $1.96 \text{ \AA}$ , respectively. Based on the above results, Fe atoms are atomically immobilized in Fe<sub>x</sub>P/HPC with Fe–N and axial Fe–O bonds in the first coordination sphere (Figures 2h, S7, and Table S1).<sup>45</sup>

**Electrocatalytic Performance.** The ORR performance of Fe<sub>x</sub>P/HPC was systematically evaluated in an O<sub>2</sub>-saturated 0.1 M KOH utilizing rotating disk electrode (RDE) and rotating ring-disk electrode (RRDE) techniques. The cyclic voltammetry (CV) curves in Figure S8 demonstrate that Fe<sub>x</sub>P/HPC has the most positive redox peak potential at 0.85 V compared to those of Fe/HPC (0.82 V), P/HPC (0.76 V), and Pt/C (0.84 V), indicating the best catalytic ORR performance.<sup>46</sup> Linear sweep voltammetry (LSV) shows that Fe<sub>x</sub>P/HPC exhibits a half-wave potential ( $E_{1/2}$ ) of 0.92 V (Figure 3a). These values significantly exceed those of Fe/HPC (0.89 V), P/HPC (0.84 V), Pt/C (0.85 V), and most of the reported Fe SACs (Table S2), which suggests that the synergistic effect between metal–nonmetal catalytic pairs may play a significant role. Furthermore, Fe<sub>x</sub>P/HPC exhibits a significant kinetic current density ( $J_k$ ) of 44 mA cm<sup>-2</sup> at 0.85 V, representing a 1.9-fold enhancement compared to that of Pt/C (24 mA cm<sup>-2</sup>, Figure 3b). Compared to Fe/HPC (65.7 mV dec<sup>-1</sup>), P/HPC (90.0 mV dec<sup>-1</sup>), and Pt/C (66.7 mV dec<sup>-1</sup>), Fe<sub>x</sub>P/HPC displays a lower Tafel slope (58.9 mV dec<sup>-1</sup>), confirming the fast kinetics in ORR (Figure 3c). The Kouteck–Levich (K–L) diagram reveals that the electron transfer number of Fe<sub>x</sub>P/HPC approaches four (Figure 3d). In addition, RRDE measurements further confirm that the ORR on Fe<sub>x</sub>P/HPC follows a dominant four-electron pathway. The hydrogen peroxide yield (H<sub>2</sub>O<sub>2</sub>%) is below 0.66% within the potential range of 0.2–0.8 V, significantly lower than that of commercial Pt/C, demonstrating the high four-electron ORR selectivity of Fe<sub>x</sub>P/HPC (Figures S9 and S10). Moreover, Fe<sub>x</sub>P/HPC possesses a larger electrochemical double-layer capacitance ( $C_{dl}$ , 21.21 mF cm<sup>-2</sup>) than Pt/C (10.17 mF cm<sup>-2</sup>), which facilitates exposure of active sites in Fe<sub>x</sub>P/HPC (Figures S11 and S12).<sup>47</sup> The active site density (SD) of the Fe<sub>x</sub>P/HPC was

quantified using an in situ electrochemical nitrite poisoning technique.<sup>48</sup> As shown in Figure S13, the SD of Fe<sub>x</sub>P/HPC reaches as high as  $6.29 \times 10^{19}$  sites g<sup>-1</sup>.

Fe<sub>x</sub>P/HPC shows only an 8 mV decay in  $E_{1/2}$  after 30,000 cycles (Figure S14). In addition, Fe<sub>x</sub>P/HPC maintains approximately 90% of its initial activity, even after 150 h. In contrast, Pt/C exhibits a significant 16.8% current density decay after only 20 h of chronoamperometry (i–t) measurement (Figure 3e), demonstrating the stability of Fe<sub>x</sub>P/HPC. The morphological structure of Fe<sub>x</sub>P/HPC remains intact after ADT (Figure S15). EDX mapping images of Fe<sub>x</sub>P/HPC after ADT reveal a homogeneous distribution of C, N, P, and Fe (Figures S16 and S17). The HAADF-STEM images (Figure S18) show that the atomic dispersion of Fe is maintained after an accelerated degradation test (ADT). The XRD pattern of Fe<sub>x</sub>P/HPC after the ADT test demonstrates that it has structural stability (Figure S19). Furthermore, the XPS spectra (Figure S20) and elemental analysis (Table S3) indicate negligible changes in the chemical states and contents of Fe, P, N, and C. Notably, the Fe content in Fe<sub>x</sub>P/HPC after ADT is 0.45 wt % with negligible loss, demonstrating the high structural stability and antidecomposition capability. In addition, the RRDE values of Fe<sub>x</sub>P/HPC, Fe/HPC, and P/HPC are displayed in Figure S21. The results indicate that the H<sub>2</sub>O<sub>2</sub>% of Fe<sub>x</sub>P/HPC (below 0.66%) is significantly lower than those of Fe/HPC (~3.3%) and P/HPC (~3.1%) within the potential range of 0.2–0.8 V. To assess the potential for carbon corrosion, we further evaluated the Fenton reactivity of the catalysts using 2,2'-azinobis (3-ethylbenzothiazoline-6-sulfonate) (ABTS) as a probe, which is oxidized by reactive oxygen species (ROS) to generate a characteristic absorbance change at 417 nm.<sup>49</sup> According to ultraviolet–visible absorbance spectroscopy (UV–vis) absorption spectrometry (Figure S22), the absorbance of Fe<sub>x</sub>P/HPC is strikingly lower than that of Fe/HPC. The result confirms that the introduction of phosphorus effectively suppresses the generation of ·OH radicals. Consequently, this in turn mitigates the oxidative corrosion of both the carbon support and the active sites, thereby greatly enhancing the durability of the catalyst.<sup>50</sup> When methanol is introduced into 0.1 M KOH, Fe<sub>x</sub>P/HPC maintains a nearly unchanged performance, while Pt/C shows a sharp activity decline (Figure 3f). The methanol resistance makes Fe<sub>x</sub>P/HPC particularly valuable for use in methanol fuel cells. The enhanced stability of Fe<sub>x</sub>P/HPC originates from the synergistic combination of stable Fe–N<sub>4</sub> coordination, P-induced suppression of destructive Fenton reactions, and the inherent robustness of the hierarchical porous carbon support.

Notably, Fe<sub>x</sub>P/HPC exhibits ORR activity in O<sub>2</sub>-saturated 0.1 M HClO<sub>4</sub>. Fe<sub>x</sub>P/HPC achieves a high  $E_{1/2}$  of 0.74 V, outperforming Fe/HPC (0.70 V) and P/HPC (0.67 V, Figure 3g). Fe<sub>x</sub>P/HPC shows a Tafel slope of 64.8 mV dec<sup>-1</sup>, which is lower than that of Pt/C (68.3 mV dec<sup>-1</sup>), indicating faster catalytic kinetics in acidic media (Figure S23). Moreover, the i–t test demonstrates the enhanced stability of Fe<sub>x</sub>P/HPC over a 20 h period with a current density retention of 94.2% (Figure 3h). It is worth noting that Fe<sub>x</sub>P/HPC also possesses good methanol tolerance capacity in 0.1 M HClO<sub>4</sub> (Figure S24). Based on the above results, Fe<sub>x</sub>P/HPC exhibits ORR performance in acidic media, indicating promising potential as a cathode catalyst for proton-exchange membrane fuel cells (PEMFCs).

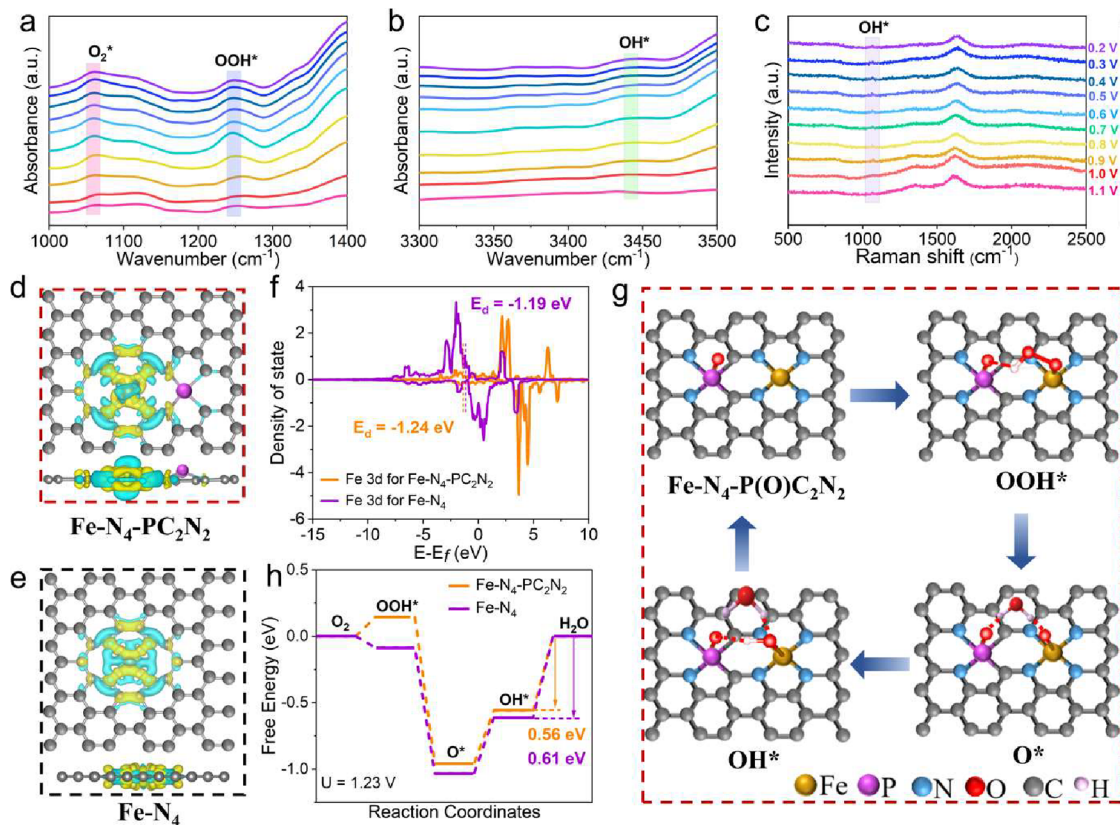


**Figure 4.** (a, b) In situ FTIR spectra. (c) In situ Raman spectra of Fe<sub>x</sub>P/HPC during ORR. Charge density difference diagrams of (d) Fe-N<sub>4</sub>-PC<sub>2</sub>N<sub>2</sub> and (e) Fe-N<sub>4</sub> (yellow: electron accumulation; cyan: electron depletion). (f) PDOS of Fe-N<sub>4</sub>-PC<sub>2</sub>N<sub>2</sub> and Fe-N<sub>4</sub>. (g) Adsorption configurations of ORR intermediates on Fe-N<sub>4</sub>-PC<sub>2</sub>N<sub>2</sub>. (h) Gibbs free-energy diagrams of Fe-N<sub>4</sub>-PC<sub>2</sub>N<sub>2</sub> and Fe-N<sub>4</sub> under an electrode potential of  $U = 1.23$  V.

As revealed by the oxygen evolution reaction (OER) polarization curves (Figure 3i), Fe<sub>x</sub>P/HPC exhibits enhanced catalytic activity in 1.0 M KOH. It is much lower than those of Fe/HPC (431 mV) and P/HPC (471 mV), achieving a current density of 10 mA cm<sup>-2</sup> at a low overpotential ( $\eta$ ) of 367 mV and approaching the performance of the RuO<sub>2</sub> benchmark (357 mV). Furthermore, Fe<sub>x</sub>P/HPC possesses a Tafel slope of 64 mV dec<sup>-1</sup>, comparable to that of RuO<sub>2</sub> (59 mV dec<sup>-1</sup>), indicating the faster OER kinetics of Fe<sub>x</sub>P/HPC (Figure S25). The chronoamperometric measurement displays that the relative current density remains 91% even after 30 h for Fe<sub>x</sub>P/HPC, outperforming the benchmark RuO<sub>2</sub> (Figure S26). Therefore, Fe<sub>x</sub>P/HPC is illustrated as an efficient bifunctional ORR/OER electrocatalyst.

**Theoretical Insights.** To gain deeper insights into the reaction mechanism of Fe<sub>x</sub>P/HPC, in situ Fourier transform infrared (FTIR) spectroscopy and in situ Raman spectroscopy were employed. As the potential decreased, three distinct infrared absorption bands emerged at 1060, 1248, and 3445 cm<sup>-1</sup>, which are attributed to O<sub>2</sub><sup>\*</sup>, OOH<sup>\*</sup>, and OH<sup>\*</sup> species, respectively (Figure 4a,b).<sup>51</sup> The presence of the key intermediate OOH<sup>\*</sup> confirms a typical four-electron ORR pathway.<sup>18,52</sup> Notably, the increasing absorbance at 3445 cm<sup>-1</sup> with decreasing potential indicates the progressive accumulation of OH<sup>\*</sup> intermediates on the active sites, suggesting that OH<sup>\*</sup> desorption may be the rate-determining step (RDS). The in situ Raman spectra reveal that at the initial high potential Fe<sub>x</sub>P/HPC only exhibits characteristic peaks of carbon (D-band around: 1344 cm<sup>-1</sup>; G-band around 1585 cm<sup>-1</sup>; Figure

4c). As the potential decreases, a new Raman peak emerges at approximately 1060 cm<sup>-1</sup>, corresponding to surface OH species.<sup>53</sup> Critically, the intensity of this peak reaches a maximum at about 0.7 V before declining, demonstrating the efficient reduction and desorption of adsorbed OH species facilitated by Fe<sub>x</sub>P/HPC. These results collectively prove that Fe<sub>x</sub>P/HPC optimizes OH<sup>\*</sup> adsorption/desorption dynamics, thereby accelerating the ORR kinetics.

To further elucidate the underlying ORR mechanism on Fe<sub>x</sub>P/HPC, DFT calculations were performed. Based on the XPS and EXAFS analyses, 10 possible configurations were constructed (Figure S27 and Table S4). The energetically optimal configuration is identified as Fe-N<sub>4</sub>-PC<sub>2</sub>N<sub>2</sub>, where P atoms exhibit strong O affinity while Fe atoms serve as the primary adsorption sites for ORR intermediates.<sup>54,55</sup> Notably, when an O atom is introduced near the P site, the ORR intermediates form various hydrogen-bonding networks with both Fe and P atoms in the second coordination shell.<sup>32,34,35</sup> This hydrogen bonding, facilitated by dual-site synergy, stabilized and activated key intermediates (e.g., OOH<sup>\*</sup>, O<sup>\*</sup>, OH<sup>\*</sup>), thereby accelerating the ORR cycle.<sup>33,36</sup> Therefore, the optimized computational modeling is Fe-N<sub>4</sub>-PC<sub>2</sub>N<sub>2</sub> with P-O species (denoted as Fe-N<sub>4</sub>-PC<sub>2</sub>N<sub>2</sub>; Figure S28a). Besides, the single-site Fe-N<sub>4</sub> configuration was constructed as a comparative model (Figure S28b).

To gain deeper mechanistic insight into the electronic effect of P, we performed Bader charge and projected density of states (PDOS) analyses. The Bader charge of the Fe center increases from 1.08 e in Fe-N<sub>4</sub> to 1.23 e in Fe-N<sub>4</sub>-PC<sub>2</sub>N<sub>2</sub>

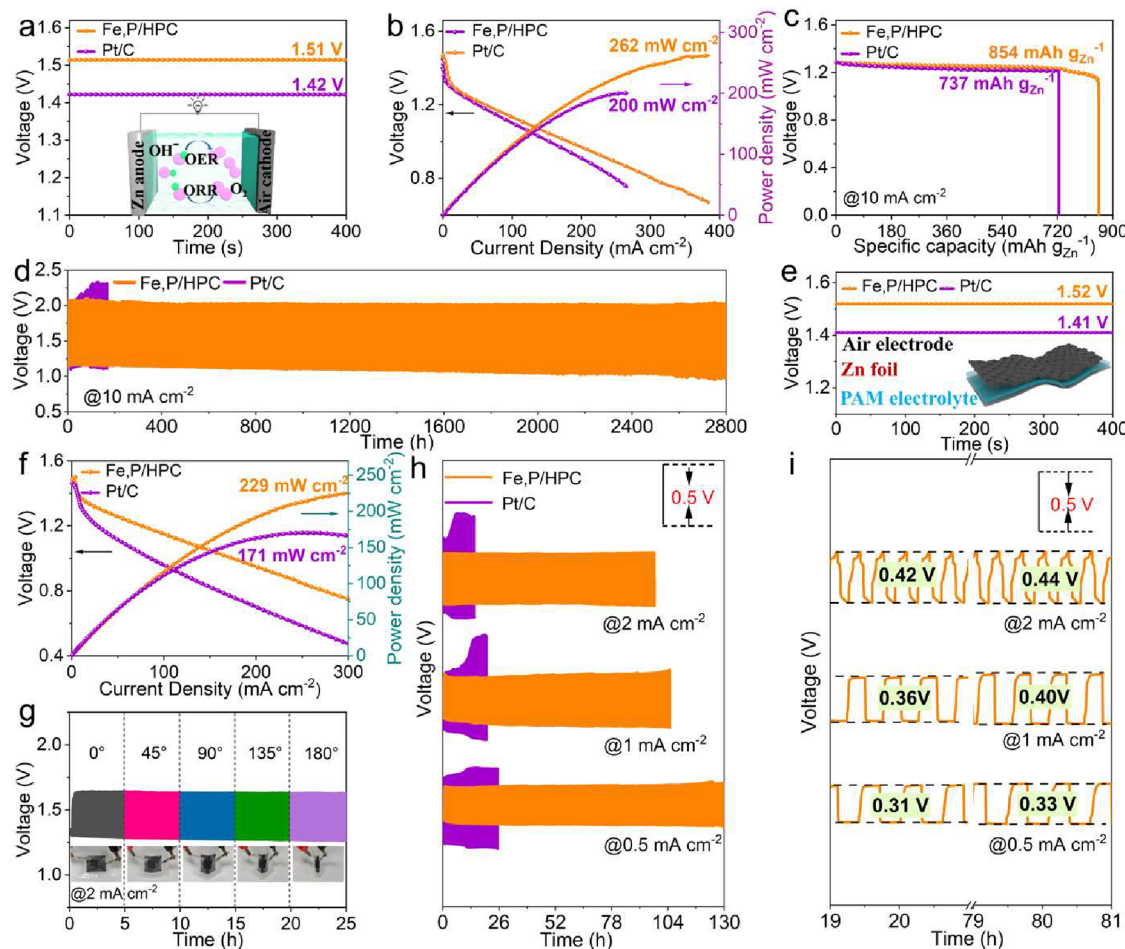


**Figure 5.** (a) OCV curves. (b) Discharge polarization curves and the corresponding power density curves of Fe,P/HPC and Pt/C-based A-ZABs. (c) Specific capacity of A-ZAB using Fe,P/HPC and Pt/C, and the discharge current density is  $10 \text{ mA cm}^{-2}$ . (d) Galvanostatic charge–discharge cycling curves of A-ZAB using Fe,P/HPC and Pt/C. (e) OCVs of QSS-ZAB assembled with Fe,P/HPC and Pt/C, respectively. (f) Discharge polarization curves and the corresponding power density curves of Fe,P/HPC and Pt/C-based QSS-ZABs. (g) Galvanostatic charge–discharge cycling curve of Fe,P/HPC-based QSS-ZAB under different bending conditions. (h) Galvanostatic charge–discharge cycling curves of QSS-ZAB using Fe,P/HPC and Pt/C at 0.5, 1, and  $2 \text{ mA cm}^{-2}$ , respectively. (i) Corresponding charge–discharge voltage gap.

(Figure 4d,e), signifying enhanced charge transfer from Fe to P, which weakens the adsorption of ORR intermediates.<sup>56</sup> Concurrently, PDOS calculations reveal a corresponding downshift of the Fe d-band center from  $-1.19 \text{ eV}$  of  $\text{Fe}-\text{N}_4$  to  $-1.24 \text{ eV}$  of  $\text{Fe}-\text{N}_4-\text{PC}_2\text{N}_2$  (Figure 4f). The downshifted d-band center, resulting from increased electron occupancy in Fe antibonding orbitals, directly explains the optimized adsorption energy.<sup>57</sup> Together, these findings demonstrate that P doping tunes the electronic structure of Fe, effectively reducing the adsorption strength of the ORR intermediates on the Fe sites.

The Gibbs free-energy diagrams for the ORR on  $\text{Fe}-\text{N}_4-\text{PC}_2\text{N}_2$  and  $\text{Fe}-\text{N}_4$  are shown in Figures 4g and S29. When  $U = 0 \text{ V}$ , all of the proton-coupled electron transfer (PCET) steps are thermodynamically spontaneous in both  $\text{Fe}-\text{N}_4-\text{PC}_2\text{N}_2$  and  $\text{Fe}-\text{N}_4$  configurations (Figure S30). However, the weaker binding strengths of  $\text{O}^*$  and  $\text{OH}^*$  on  $\text{Fe}-\text{N}_4-\text{PC}_2\text{N}_2$  than those of the  $\text{Fe}-\text{N}_4$  configuration suggest the easier  $\text{O}^*$  and  $\text{OH}^*$  desorption. At the equilibrium potential ( $U = 1.23 \text{ V}$ ), the  $\text{O}_2 \rightarrow \text{OOH}^*$ , the  $\text{O}^* \rightarrow \text{OH}^*$ , and the  $\text{OH}^* \rightarrow \text{H}_2\text{O}$  PCET steps become endergonic for  $\text{Fe}-\text{N}_4-\text{PC}_2\text{N}_2$  (Figure 4h). For the  $\text{Fe}-\text{N}_4$  configuration, the last two PCET steps are

endothermic. Observably, the RDS for both configurations is  $\text{OH}^* \rightarrow \text{H}_2\text{O}$ , but  $\text{Fe}-\text{N}_4-\text{PC}_2\text{N}_2$  exhibits a lower energy barrier ( $0.56$  vs  $0.61 \text{ eV}$  for  $\text{Fe}-\text{N}_4$ ), confirming that P site incorporation promoted  $\text{OH}^*$  desorption. We attribute this enhancement to the hydrogen-bonding interactions between P–O species and oxygen intermediates adsorbed on Fe sites, which optimizes the adsorption strengths of the intermediates and lowers the RDS energy barrier of  $\text{OH}^*$  desorption.

Our results demonstrate that the Fe–P heteronuclear pair operates through a distinct mechanism that sets it apart from other reported systems such as Fe–S or Fe–B. While the latter primarily adjusts the electronic properties of the Fe site, the Fe–P synergy uniquely introduces a hydrogen-bonding regulatory function. This dual role of electronic modulation coupled with direct stabilization of intermediates via hydrogen bonding provides a more powerful strategy for optimizing multistep catalytic reactions such as the ORR. Comprehensively, synergistic Fe–P metal–nonmetal catalytic pairs accelerate ORR kinetics, consistent with the enhanced experimental ORR performance of Fe,P/HPC.

**ZAB Performance.** To evaluate the practical application of Fe,P/HPC, we assembled an A-ZAB using Fe,P/HPC as the

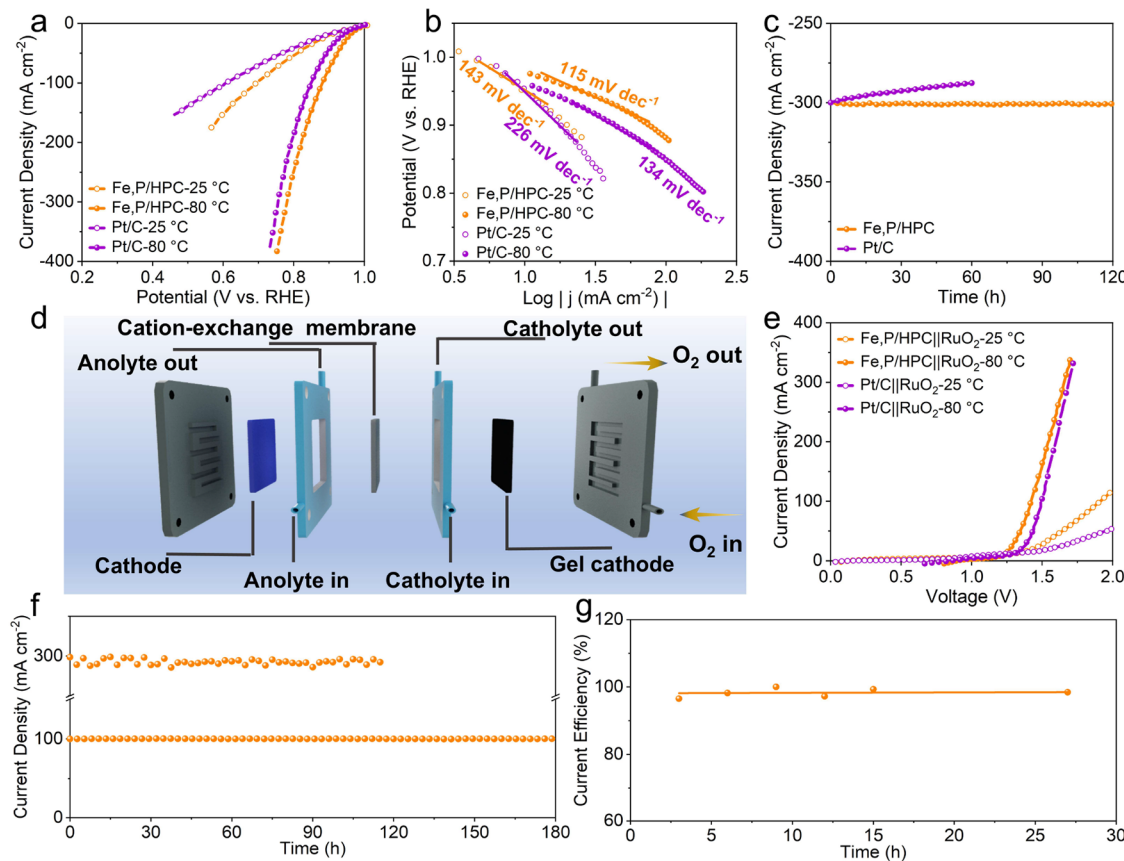


**Figure 6.** (a) ORR LSV curves of Fe,P/HPC- and Pt/C-based ODCs recorded in 30 wt % NaOH solution at 25 and 80 °C, respectively. (b) Tafel plots of Fe,P/HPC- and Pt/C-based ODCs at 25 and 80 °C, respectively. (c) Chronoamperometric curves of Fe,P/HPC- and Pt/C-based ODCs recorded in 30 wt % NaOH solution at 80 °C. (d) Schematic illustration of a two-electrode flow cell that simulates the industrial chlor-alkali process. (e) LSV curves of Fe,P/HPC||RuO<sub>2</sub> and Pt/C||RuO<sub>2</sub> two-electrode flow cells measured at 25 and 80 °C, respectively. (f) Chronoamperometric response of Fe,P/HPC||RuO<sub>2</sub> two-electrode flow cell. (g) Caustic current efficiency of Fe,P/HPC||RuO<sub>2</sub> two-electrode flow cell calculated at 300 mA cm<sup>-2</sup>.

air electrode catalyst, a Zn plate as the anode, and a mixed solution (6 M KOH + 0.2 M Zn(Ac)<sub>2</sub>) as the electrolyte. A Pt/C-based A-ZAB was used as the reference. As expected, the Fe,P/HPC-based A-ZAB exhibits a large OCV of 1.51 V (Figure 5a) and a high power density of 262 mW cm<sup>-2</sup> (Figure 5b), outperforming Pt/C-based A-ZAB (1.42 V; 200 mW cm<sup>-2</sup>) and recently reported state-of-the-art Fe SACs (Table S5). Moreover, Fe,P/HPC-based A-ZAB delivers a specific capacity of 854 mAh g<sup>-1</sup> at 10 mA cm<sup>-2</sup> (Figure 5c), which is higher than that of Pt/C-based A-ZAB (737 mAh g<sup>-1</sup> at 10 mA cm<sup>-2</sup>). The rate capability of Fe,P/HPC-based A-ZAB in Figure S31 shows a high output voltage at all current densities (from 2 to 50 mA cm<sup>-2</sup>). Notably, at 50 mA cm<sup>-2</sup>, Fe,P/HPC-based A-ZAB achieves a discharge voltage of 1.18 V. When the current density is reduced to 5 mA cm<sup>-2</sup>, A-ZAB assembled by Fe,P/HPC maintains its initial potential, indicating an enhanced rate performance. Fe,P/HPC-based A-ZAB demonstrates stable charge–discharge cycling for 2800 h with a small voltage gap at 10 mA cm<sup>-2</sup> (Figure 5d and Figure S32a). Notably, it exhibits good voltage efficiency during 500–2500 h of cycling, showing merely a 3.68% decline (from 55.66 to 51.98%, Figure S32b).

LSV curves reveal a significant overpotential decrease of 235 mV at 10 mA cm<sup>-2</sup> after KI addition in 1.0 M KOH (Figure S33). The lowered potential unequivocally demonstrates the pivotal role of Fe,P/HPC in catalyzing the I<sup>-</sup> oxidation to

I<sup>-</sup>.<sup>58</sup> This iodide oxidation reaction, being thermodynamically more favorable, effectively suppresses the competing multielectron OER pathway.<sup>5</sup> Therefore, a QSS-ZAB was fabricated employing a KOH/Zn(Ac)<sub>2</sub>/KI-impregnated polyacrylamide (PAM) electrolyte.<sup>59</sup> The Fe,P/HPC-based QSS-ZAB achieves a high OCV of 1.52 V compared with the Pt/C-based QSS-ZAB (1.41 V, Figure 5e). Fe,P/HPC-based QSS-ZAB delivers a peak power density of 229 mW cm<sup>-2</sup>, outperforming Pt/C-based one (171 mW cm<sup>-2</sup>) and recently reported Fe SACs (Figure 5f, Table S6). Moreover, Fe,P/HPC-based QSS-ZAB delivers a specific capacity of 781 mAh g<sup>-1</sup> at 2 mA cm<sup>-2</sup> (Figure S34), surpassing Pt/C-based system (719 mAh g<sup>-1</sup>). Fe,P/HPC-based QSS-ZAB maintains higher discharge voltages than Pt/C-based QSS-ZAB at all current densities of 0.5, 1, 2, 5, and 10 mA cm<sup>-2</sup>. Even at 10 mA cm<sup>-2</sup>, it achieves a discharge voltage of 1.30 V, surpassing that of the Pt/C system. These results demonstrate the enhanced rate performance of Fe,P/HPC-based QSS-ZAB (Figure S35). In addition, Fe,P/HPC-based QSS-ZAB maintains a stable cycling performance without significant capacity loss under all bending conditions (Figure 5g).

Notably, Fe,P/HPC-based QSS-ZAB demonstrates better charge–discharge cycling stability than the Pt/C-based one, maintaining stable operation for 130 h at 0.5 mA cm<sup>-2</sup>, 100 h at 1 mA cm<sup>-2</sup>, and 95 h at 2 mA cm<sup>-2</sup>, respectively (Figure 5h). At 0.5 mA cm<sup>-2</sup>, Fe,P/HPC-based QSS-ZAB maintains a

small charge–discharge voltage gap of 0.31 V after 20 h, which increases only marginally to 0.33 V after 80 h of operation (Figure 5i). The corresponding voltage conversion efficiencies are 79.6 and 78.08% at 20 and 80 h, respectively. Under a constant current density of 1 mA cm<sup>-2</sup>, the charge–discharge voltage gap of Fe<sub>x</sub>P/HPC-based QSS-ZAB demonstrates a minimal increase from 0.36 V at 20 h to 0.40 V at 80 h, with the voltage conversion efficiency showing only a slight decrease from 75.84 to 73.50%. Even under a high current density of 2 mA cm<sup>-2</sup>, Fe<sub>x</sub>P/HPC-based QSS-ZAB exhibits merely a 20 mV increase in the charge–discharge voltage gap, corresponding to a 0.5% decrease in the voltage conversion efficiency. All in all, Fe<sub>x</sub>P/HPC-based QSS-ZAB combines enhanced stability, mechanical flexibility, and prolonged cycling durability, positioning it as a highly promising energy storage solution for next-generation wearable and portable electronic applications.

**ODC-Based Chlor-Alkali Electrolyzer.** The electrochemical performance of Fe<sub>x</sub>P/HPC for the chlor-alkali electrolyzer was evaluated using an ODC system in a 30 wt % NaOH aqueous solution. The Fe<sub>x</sub>P/HPC-based ODC exhibits significantly enhanced ORR activity compared to its Pt/C-based counterpart at both 25 and 80 °C (Figure 6a). Specifically, Fe<sub>x</sub>P/HPC requires 0.69 V to reach a current density of 100 mA cm<sup>-2</sup> at 25 °C, outperforming Pt/C (0.60 V). At an elevated temperature (80 °C), the advantage is more pronounced. Fe<sub>x</sub>P/HPC-based ODC requires a potential of 0.78 V at 300 mA cm<sup>-2</sup>, significantly higher than that of Pt/C (0.76 V at 300 mA cm<sup>-2</sup>). Moreover, the Tafel slope of Fe<sub>x</sub>P/HPC-based ODC is 115 mV dec<sup>-1</sup> (Figure 6b), much lower than that of Pt/C-based ODC (134 mV dec<sup>-1</sup>), indicating the more favorable reaction dynamics of Fe<sub>x</sub>P/HPC-based ODC. Surprisingly, Fe<sub>x</sub>P/HPC-based ODC sustains more than 120 h of continuous operation at a large current density of 300 mA cm<sup>-2</sup> and 80 °C (Figure 6c), confirming its long-term stability for potential industrial chlor-alkali applications.

To evaluate the activity and stability of Fe<sub>x</sub>P/HPC in the chlor-alkali electrolyzer, we assembled a two-electrode flow cell with the Fe<sub>x</sub>P/HPC-based ODC and RuO<sub>2</sub> anode (denoted as Fe<sub>x</sub>P/HPC||RuO<sub>2</sub>, Figure 6d). For comparison, a reference cell was prepared using a Pt/C-based ODC with an identical RuO<sub>2</sub> anode (Pt/C||RuO<sub>2</sub>). When operating at 25 °C, Fe<sub>x</sub>P/HPC||RuO<sub>2</sub> system achieves 50 mA cm<sup>-2</sup> at a cell voltage of only 1.65 V, 0.31 V lower than Pt/C||RuO<sub>2</sub> (1.96 V, Figure 6e). At 80 °C, Fe<sub>x</sub>P/HPC||RuO<sub>2</sub> reaches 300 mA cm<sup>-2</sup> at only 1.66 V, superior to its Pt/C||RuO<sub>2</sub> counterpart (1.70 V @ 300 mA cm<sup>-2</sup>). Additionally, Fe<sub>x</sub>P/HPC||RuO<sub>2</sub> also exhibits enhanced durability, maintaining its stable operation at 100 mA cm<sup>-2</sup> for 180 h (Figure 6f). Specifically, even at a large current density of 300 mA cm<sup>-2</sup>, it can work stably for more than 110 h, confirming robust stability under industrial conditions. Notably, the caustic current efficiency of Fe<sub>x</sub>P/HPC||RuO<sub>2</sub> is maintained at approximately 100% throughout the entire testing period at 300 mA cm<sup>-2</sup> (Figure 6g), suggesting negligible side reactions. These results underscore the strong competitiveness of Fe<sub>x</sub>P/HPC as an ODC catalyst for the industrial chlor-alkali electrolyzer.

## CONCLUSIONS

In conclusion, we successfully immobilized Fe and P heteronuclear catalytic pairs on hierarchical porous carbon through transition metal complex adsorption and thermal activation strategy. DFT calculations show that hydrogen-bond

interactions between the Fe and P heteronuclear catalytic pairs optimize the binding strength of oxygen intermediates and lower the RDS barrier of OH\* desorption, endowing Fe<sub>x</sub>P/HPC with enhanced ORR kinetics. Thus, Fe<sub>x</sub>P/HPC achieves an  $E_{1/2}$  of 0.92 V in 0.1 M KOH and enhanced stability, maintaining 90% retention of the initial current density for over 150 h operation. In addition, Fe<sub>x</sub>P/HPC achieves good ORR and OER performances in 0.1 M HClO<sub>4</sub> and 1.0 M KOH, respectively. Fe<sub>x</sub>P/HPC-based A-ZAB delivers a high power density of 262 mW cm<sup>-2</sup> and an ultralong cycling durability with a small voltage gap after over 2800 h. Moreover, QSS-ZAB based on Fe<sub>x</sub>P/HPC achieves a large OCV of 1.52 V and sustains stable charge–discharge cycling for 95 h at current densities of 0.5, 1, and 2 mA cm<sup>-2</sup>, respectively, with negligible voltage efficiency loss. Notably, Fe<sub>x</sub>P/HPC||RuO<sub>2</sub> chlor-alkali electrolyzer achieves a current density of 300 mA cm<sup>-2</sup> at only 1.66 V and delivers negligible attenuation during a 110 h chronoamperometric test. In addition, the caustic current efficiency of Fe<sub>x</sub>P/HPC||RuO<sub>2</sub> is around 100% throughout the entire testing period at 300 mA cm<sup>-2</sup>. This work demonstrates that atomic-level heteronuclear metal–nonmetal catalytic pairs provide a paradigm for designing efficient and durable electrocatalysts, advancing the development of metal–air batteries and industrial electrolyzers.

## EXPERIMENTAL SECTION

**Chemicals.** NaNO<sub>3</sub>, C<sub>6</sub>H<sub>12</sub>O<sub>6</sub>, C<sub>3</sub>H<sub>6</sub>N<sub>6</sub>, C<sub>6</sub>H<sub>18</sub>O<sub>23</sub>P<sub>6</sub>, C<sub>4</sub>H<sub>6</sub>O<sub>4</sub>Fe, 1,10-phenanthroline, acrylamide (AM), N,N'-methylenebis (MBA), polytetrafluoroethylene preparation (60 wt %), polytetrafluoroethylene (PTFE), and sodium citrate were bought from Aladdin. Nafion 117 solution, Pt/C (20 wt %), and RuO<sub>2</sub> were purchased from Sigma-Aldrich. K<sub>2</sub>S<sub>2</sub>O<sub>8</sub> (analytical grade), C<sub>4</sub>H<sub>6</sub>O<sub>4</sub>Zn·2H<sub>2</sub>O (analytical grade), KI (analytical grade), KOH (analytical grade), HClO<sub>4</sub> (analytical grade), and C<sub>2</sub>H<sub>5</sub>OH (analytical grade) were bought from Sinopharm Chemical Reagent Co. Ltd. Carbon black (BP2000) was supplied by Suzhou Yilongsheng Energy Technology Co. Ltd. The Nafion 424 ion-exchange membrane was purchased from Suzhou Shengernuo Co. Ltd. The deionized water in the experiment is always ultrapure water (18.2 MΩ cm).

**Synthesis of HPC.** First, 1.2 g of NaNO<sub>3</sub>, 2.4 g of C<sub>6</sub>H<sub>12</sub>O<sub>6</sub>, and 1.2 g of C<sub>3</sub>H<sub>6</sub>N<sub>6</sub> were added to 30 mL of water, and the mixture was stirred for 10 min. Then, 5 mL of 0.5 M HCl was injected into the mixed solution to form a gel. The gel was subjected to hydrothermal treatment at 120 °C for 12 h. After cooling, the solid residue was collected and dried via lyophilization. Finally, the dried sample was loaded into a tube furnace under a N<sub>2</sub> atmosphere. The sample was heated to 900 °C at a rate of 3 °C min<sup>-1</sup> and then kept at that temperature for 1 h. The carbonized sample was thoroughly washed with deionized water and freeze-dried to obtain HPC.

**Synthesis of P/HPC.** With the exception of the addition of 1 mL of C<sub>6</sub>H<sub>18</sub>O<sub>23</sub>P<sub>6</sub> during the hydrothermal treatment, P/HPC was synthesized following the same procedure as that for HPC.

**Synthesis of Fe<sub>x</sub>P/HPC.** First, 1 mL of iron acetate (10 mg mL<sup>-1</sup> in ethanol), 34.2 mg of 1,10-phenanthroline, and 50 mg of P/HPC were added to 20 mL of ethanol in a flask, and the mixture was stirred until completely dissolved. Then, the reaction mixture was heated in an oil bath at 65 °C for 4 h. After cooling, the solid residue was transferred to an oven and dried at 60 °C for 24 h. The dried sample was loaded into a tube furnace under a N<sub>2</sub> atmosphere. It was heated to 150 °C at a rate of 10 °C min<sup>-1</sup> and maintained at that temperature for 1 h. It was then reheated to 900 °C at the same rate and maintained for 2 h. Finally, the obtained sample was stirred in 0.5 M H<sub>2</sub>SO<sub>4</sub> overnight. It was washed thoroughly with deionized water and dried to obtain the final product, denoted as Fe<sub>x</sub>P/HPC.

**Synthesis of Fe/HPC.** The synthesis procedure for Fe/HPC was identical to that of Fe<sub>x</sub>P/HPC, with the exception that HPC was used as the carbon support instead of P/HPC.

## ASSOCIATED CONTENT

### Supporting Information

The Supporting Information is available free of charge at <https://pubs.acs.org/doi/10.1021/acsnano.5c15715>.

Experimental details, electrochemical test method, computational methods, SEM and TEM images, XRD patterns, Raman spectra, N<sub>2</sub> sorption isotherms, XPS spectra, EXAFS fittings, electrochemical performance, ZAB performance, and additional data. This material is available free of charge ([PDF](#))

## AUTHOR INFORMATION

### Corresponding Authors

Lingbo Zong – State Key Laboratory of Eco-chemical Engineering and College of Chemistry and Molecular Engineering, Qingdao University of Science and Technology, Qingdao 266042, China;  [orcid.org/0000-0002-4053-0570](https://orcid.org/0000-0002-4053-0570); Email: [lingbozong@qust.edu.cn](mailto:lingbozong@qust.edu.cn)

Zumin Wang – Key Laboratory of Biopharmaceutical Preparation and Delivery, Institute of Process Engineering, Chinese Academy of Sciences, Beijing 100190, China;  [orcid.org/0000-0002-0732-787X](https://orcid.org/0000-0002-0732-787X); Email: [wangzm@ipe.ac.cn](mailto:wangzm@ipe.ac.cn)

Lei Wang – State Key Laboratory of Eco-chemical Engineering and College of Chemistry and Molecular Engineering, Qingdao University of Science and Technology, Qingdao 266042, China;  [orcid.org/0000-0001-7275-4846](https://orcid.org/0000-0001-7275-4846); Email: [inorchemwl@126.com](mailto:inorchemwl@126.com)

Bin Li – State Key Laboratory of Eco-chemical Engineering and College of Materials Science and Engineering, Qingdao University of Science and Technology, Qingdao 266042, China; Email: [binli@qust.edu.cn](mailto:binli@qust.edu.cn)

### Authors

Fenghong Lu – State Key Laboratory of Eco-chemical Engineering and College of Environment and Safety Engineering, Qingdao University of Science and Technology, Qingdao 266042, China

Yuanyuan Zhang – State Key Laboratory of Eco-chemical Engineering and College of Chemistry and Molecular Engineering, Qingdao University of Science and Technology, Qingdao 266042, China

Chengbin Wang – State Key Laboratory of Eco-chemical Engineering and College of Chemistry and Molecular Engineering, Qingdao University of Science and Technology, Qingdao 266042, China

Kaicai Fan – State Key Laboratory of Eco-chemical Engineering and College of Chemistry and Molecular Engineering, Qingdao University of Science and Technology, Qingdao 266042, China;  [orcid.org/0000-0001-9995-7192](https://orcid.org/0000-0001-9995-7192)

Cheng-Hao Chuang – Department of Physics, Tamkang University, New Taipei City 251, Taiwan;  [orcid.org/0000-0001-8161-1521](https://orcid.org/0000-0001-8161-1521)

Porun Liu – Centre for Catalysis and Clean Energy, School of Environment and Science, Griffith University, Gold Coast, Queensland 4222, Australia;  [orcid.org/0000-0002-0046-701X](https://orcid.org/0000-0002-0046-701X)

Complete contact information is available at: <https://pubs.acs.org/doi/10.1021/acsnano.5c15715>

## Author Contributions

F.L.: Investigation, data curation, writing—original draft. Y.Z.: Investigation, data curation. L.Z.: Conceptualization, supervision, investigation, writing—review and editing, funding acquisition. C.W.: Investigation, data curation. K.F.: Investigation, funding acquisition. C.-H.C.: Resources. P.L.: Resources. Z.W.: Writing—review and editing. L.W.: Supervision. B.L.: Supervision.

## Notes

The authors declare no competing financial interest.

## ACKNOWLEDGMENTS

This work was supported financially by the National Natural Science Foundation of China, China (Grant No. 52172208), the Taishan Scholar Young Talent Program (tsqn202306216), and the Shandong Excellent Young Scientists Fund Program (Overseas, 2023HWYQ-091).

## REFERENCES

- (1) Wang, Q.; Kaushik, S.; Xiao, X.; Xu, Q. Sustainable Zinc-Air Battery Chemistry: Advances, Challenges and Prospects. *Chem. Soc. Rev.* **2023**, *52* (17), 6139–6190.
- (2) Jiang, H.; He, J.; Zhou, S.; Yuan, M.; Lin, L.; Sun, Z.; Sun, G. Electron Donor–Acceptor Activated Anti-Fenton Property for the Ultradurable Oxygen Reduction Reaction. *ACS Nano* **2025**, *19* (12), 12161–12169.
- (3) Shao, X.; Gan, R.; Rao, Y.; Nga, T. T. T.; Liang, M.; Dong, C.-L.; Ma, C.; Lee, J. Y.; Li, H.; Lee, H. Main Group SnN<sub>4</sub>O Single Sites with Optimized Charge Distribution for Boosting the Oxygen Reduction Reaction. *ACS Nano* **2024**, *18* (22), 14742–14753.
- (4) Liu, S.; Meyer, Q.; Xu, D.; Cheng, Y.; Osmieri, L.; Li, X.-H.; Zhao, C. Breaking the Activity and Stability Trade-Off of Platinum-Free Catalysts for the Oxygen Reduction Reaction in Hydrogen Fuel Cells. *ACS Nano* **2025**, *19* (21), 19524–19551.
- (5) Liu, H.; Li, P.; Fan, K.; Lu, F.; Sun, Q.; Zhang, Q.; Li, B.; Shu, Y.; Zong, L.; Wang, L. Microporous Hard Carbon Support Provokes Exceptional Performance of Single Atom Electrocatalysts for Advanced Air Cathodes. *Angew. Chem., Int. Ed.* **2025**, *64* (23), No. e202501307.
- (6) Li, P.; Wang, C.; Zhang, G.; Fan, K.; Liu, Y.; Li, B.; Liu, P.; Zong, L.; Wang, L. Pre-Coordination Synthesis of Active Fe Single-Atom Catalyst Enabling Efficient and Ultralong-Life Oxygen Depolarized Cathode Applications. *Chem. Eng. J.* **2025**, *522* (15), No. 167199.
- (7) Wu, G.; Zelenay, P. Activity versus stability of atomically dispersed transition-metal electrocatalysts. *Nat. Rev. Mater.* **2024**, *9* (9), 643–656.
- (8) Qu, Q.; Mao, Y.; Ji, S.; Liao, J.; Dong, J.; Wang, L.; Wang, Q.; Liang, X.; Zhang, Z.; Yang, J.; et al. Engineering the Lewis Acidity of Fe Single-Atom Sites via Atomic-Level Tuning of Spatial Coordination Configuration for Enhanced Oxygen Reduction. *J. Am. Chem. Soc.* **2025**, *147* (8), 6914–6924.
- (9) Zeng, Y.; Li, C.; Li, B.; Liang, J.; Zachman, M. J.; Cullen, D. A.; Hermann, R. P.; Alp, E. E.; Lavina, B.; Karakalos, S.; et al. Tuning the Thermal Activation Atmosphere Breaks the Activity-Stability Trade-Off of Fe-N-C Oxygen Reduction Fuel Cell Catalysts. *Nat. Catal.* **2023**, *6* (12), 1215–1227.
- (10) Zhao, Y.; Wan, J.; Ling, C.; Wang, Y.; He, H.; Yang, N.; Wen, R.; Zhang, Q.; Gu, L.; Yang, B.; et al. Acidic Oxygen Reduction by Single-Atom Fe Catalysts on Curved Supports. *Nature* **2025**, *644*, 668–675.
- (11) Li, L.; Yuan, K.; Chen, Y. Breaking the Scaling Relationship Limit: From Single-Atom to Dual-Atom Catalysts. *Acc. Mater. Res.* **2022**, *3* (6), 584–596.
- (12) Li, R.; Wang, D. Superiority of Dual-Atom Catalysts in Electrocatalysis: One Step Further Than Single-Atom Catalysts. *Adv. Energy Mater.* **2022**, *12* (9), No. 2103564.

- (13) Zhu, Z.; Yin, H.; Wang, Y.; Chuang, C. H.; Xing, L.; Dong, M.; Lu, Y. R.; Casillas-Garcia, G.; Zheng, Y.; Chen, S.; et al. Coexisting Single-Atomic Fe and Ni Sites on Hierarchically Ordered Porous Carbon as a Highly Efficient ORR Electrocatalyst. *Adv. Mater.* **2020**, *32* (42), No. 2004670.
- (14) Sui, R.; Liu, B.; Chen, C.; Tan, X.; He, C.; Xin, D.; Chen, B.; Xu, Z.; Li, J.; Chen, W.; et al. Constructing Asymmetric Fe-Nb Diatomic Sites to Enhance ORR Activity and Durability. *J. Am. Chem. Soc.* **2024**, *146* (38), 26442–26453.
- (15) Jin, Z.; Li, P.; Meng, Y.; Fang, Z.; Xiao, D.; Yu, G. Understanding the Inter-Site Distance Effect in Single-Atom Catalysts for Oxygen Electroreduction. *Nat. Catal.* **2021**, *4* (7), 615–622.
- (16) Jia, C.; Li, B.; Yang, J.; Jiang, S.; Gu, Z.; Sun, L.; Zhong, W.; Sharman, E.; Luo, Y.; Jiang, J. Prediction of  $C_2N$ -Supported Double-Atom Catalysts with Individual/Integrated Descriptors for Electrochemical and Thermochemical  $CO_2$  Reduction. *J. Am. Chem. Soc.* **2025**, *147* (20), 16864–16875.
- (17) Yu, Y.; Zhang, Q.; Wei, S.; Qian, G.; He, Q.; Yin, W.; Min, D.; Wang, S.; Zhao, Y. O-Induced Diatomic Fe-Mo Mimetic Enzyme for Efficient Electrocatalytic Nitrogen Reduction at Universal pH. *J. Am. Chem. Soc.* **2025**, *147* (31), 28024–28034.
- (18) Tang, B.; Zhou, Y.; Ji, Q.; Zhuang, Z.; Zhang, L.; Wang, C.; Hu, H.; Wang, H.; Mei, B.; Song, F.; et al. A Janus Dual-Atom Catalyst for Electrocatalytic Oxygen Reduction and Evolution. *Nat. Synth.* **2024**, *3* (7), 878–890.
- (19) Shu, X.; Tan, D.; Wang, Y.; Ma, J.; Zhang, J. Bimetal Bridging Nitrogen Coordination in Carbon Based Electrocatalysts for pH Universal Oxygen Reduction. *Angew. Chem., Int. Ed.* **2024**, *136* (8), No. e202316005.
- (20) Chen, J.; Li, H.; Fan, C.; Meng, Q.; Tang, Y.; Qiu, X.; Fu, G.; Ma, T. Dual Single-Atomic  $Ni-N_4$  and  $Fe-N_4$  Sites Constructing Janus Hollow Graphene for Selective Oxygen Electrocatalysis. *Adv. Mater.* **2020**, *32* (30), No. 2003134.
- (21) Liu, M.; Wang, X.; Cao, S.; Lu, X.; Li, W.; Li, N.; Bu, X. H. Ferredoxin-Inspired Design of S-Synergized Fe-Fe Dual-Metal Center Catalysts for Enhanced Electrocatalytic Oxygen Reduction Reaction. *Adv. Mater.* **2024**, *36* (19), No. 2309231.
- (22) Meng, H.; Wu, B.; Zhang, D.; Zhu, X.; Luo, S.; You, Y.; Chen, K.; Long, J.; Zhu, J.; Liu, L.; et al. Optimizing Electronic Synergy of Atomically Dispersed Dual-Metal  $Ni-N_4$  and  $Fe-N_4$  Sites with Adjacent Fe Nanoclusters for High-Efficiency Oxygen Electrocatalysis. *Energy Environ. Sci.* **2024**, *17* (2), 704–716.
- (23) Ran, L.; Zhang, Y.; Tong, W.; Chen, L.; Wang, M.; Zhou, H.; Farràs, P.; Chen, S.; Qiu, X. Circumventing Radical Generation on Fe-V Atomic Pair Catalyst for Robust Oxygen Reduction and Zinc-Air Batteries. *Angew. Chem., Int. Ed.* **2025**, *64*, No. e202514542.
- (24) Liu, X.; Zhang, C.; Yao, H.; Zhen, C.; Xu, L.; Chen, K.; Fan, Z.; Wang, X.; Gu, M. D.; Huang, M.; et al. Tuning Metal-Nonmetal Atomic Pair Distance to Achieve Demagnetization Control in Single-Atom Catalysts for Seawater-Based Zn-Air Batteries. *Appl. Catal. B Environ. Energy* **2025**, *365* (15), No. 124990.
- (25) Wang, D.; Zhu, X.; Tu, X.; Zhang, X.; Chen, C.; Wei, X.; Li, Y.; Wang, S. Oxygen-Bridged Copper-Iron Atomic Pair as Dual-Metal Active Sites for Boosting Electrocatalytic NO Reduction. *Adv. Mater.* **2023**, *35* (39), No. 2304646.
- (26) Wang, Q.; Wang, H.; Cao, H.; Tung, C.-W.; Liu, W.; Hung, S.-F.; Wang, W.; Zhu, C.; Zhang, Z.; Cai, W.; et al. Atomic Metal-Non-Metal Catalytic Pair Drives Efficient Hydrogen Oxidation Catalysis in Fuel Cells. *Nat. Catal.* **2023**, *6* (10), 916–926.
- (27) Zhang, Z.; Li, F.; Xi, S.; Zheng, L.; Wang, X.; Du, B.; Chi, X.; Chen, Z.; Yang, H. B.; Zhang, L.; Li, D.; Liu, B.; Li, L.; Chen, P.; et al. Atomic Metal-Nonmetal Catalytic Pair Cooperatively Drives Efficient Enzyme-Mimetic Catalysis. *Angew. Chem., Int. Ed.* **2025**, *64*, No. e202508651.
- (28) Ni, J.; Yan, J.; Li, F.; Qi, H.; Xu, Q.; Su, C.; Sun, L.; Sun, H.; Ding, J.; Liu, B. Atomic Co-P Catalytic Pair Drives Efficient Electrochemical Nitrate Reduction to Ammonia. *Adv. Energy Mater.* **2024**, *14* (28), No. 2400065.
- (29) Ding, J.; Li, F.; Zhang, J.; Qi, H.; Wei, Z.; Su, C.; Yang, H. B.; Zhai, Y.; Liu, B. Room-Temperature Chemoselective Hydrogenation of Nitroarene over Atomic Metal-Nonmetal Catalytic Pair. *Adv. Mater.* **2024**, *36* (17), No. 2306480.
- (30) Chen, Z.; Niu, H.; Ding, J.; Liu, H.; Chen, P. H.; Lu, Y. H.; Lu, Y. R.; Zuo, W.; Han, L.; Guo, Y.; et al. Unraveling the Origin of Sulfur-Doped Fe-N-C Single-Atom Catalyst for Enhanced Oxygen Reduction Activity: Effect of Iron Spin-State Tuning. *Angew. Chem., Int. Ed.* **2021**, *133* (48), 25608–25614.
- (31) Cao, Y.; Liu, Y.; Zheng, X.; Yang, J.; Wang, H.; Zhang, J.; Han, X.; Deng, Y.; Rupprechter, G.; Hu, W. Quantifying Asymmetric Coordination to Correlate with Oxygen Reduction Activity in Fe-Based Single-Atom Catalysts. *Angew. Chem., Int. Ed.* **2025**, *64* (14), No. e202423556.
- (32) Zong, L.; Fan, K.; Li, P.; Lu, F.; Li, B.; Wang, L. Promoting Oxygen Reduction Reaction on Atomically Dispersed Fe Sites via Establishing Hydrogen Bonding with the Neighboring P Atoms. *Adv. Energy Mater.* **2023**, *13* (5), No. 2203611.
- (33) Chen, Z.; Su, X.; Ding, J.; Yang, N.; Zuo, W.; He, Q.; Wei, Z.; Zhang, Q.; Huang, J.; Zhai, Y. Boosting Oxygen Reduction Reaction with Fe and Se Dual-Atom Sites Supported by Nitrogen-Doped Porous Carbon. *Appl. Catal. B Environ. Energy* **2022**, *308* (5), No. 121206.
- (34) Li, B.; Shi, C.; Zhao, N.; Liu, E. Hydrogen-Bond-Promoted ORR Mechanism in P-Doped Fe-N-C Materials. *J. Phys. Chem. C* **2023**, *127* (2), 1023–1031.
- (35) Han, C.; Chen, Z. The Mechanism Study of Oxygen Reduction Reaction (ORR) on Non-Equivalent P, N Co-Doped Graphene. *Appl. Surf. Sci.* **2020**, *511*, No. 145382.
- (36) Bhunia, S.; Rana, A.; Roy, P.; Martin, D. J.; Pegis, M. L.; Roy, B.; Dey, A. Rational Design of Mononuclear Iron-Porphyrins for Facile and Selective  $4e^-/4H^+ O_2$  Reduction: Activation of O-O Bond by 2nd Sphere Hydrogen Bonding. *J. Am. Chem. Soc.* **2018**, *140* (30), 9444–9457.
- (37) Zhang, L.; Zong, L.; Lu, F.; Wang, C.; Liu, Z.; Qi, J.; Wang, L. Metal-Saloph Complexes Pre-Coordination for Fe Single Atom Catalyst towards Oxygen Reduction Reaction in Rechargeable Quasi-Solid-State Zn-Air Battery. *Appl. Catal. B Environ. Energy* **2025**, *370* (5), No. 125189.
- (38) Liu, S.; Li, C.; Zachman, M. J.; Zeng, Y.; Yu, H.; Li, B.; Wang, M.; Braaten, J.; Liu, J.; Meyer, H. M.; et al. Atomically Dispersed Iron Sites with a Nitrogen-Carbon Coating as Highly Active and Durable Oxygen Reduction Catalysts for Fuel Cells. *Nat. Energy* **2022**, *7* (7), 652–663.
- (39) Zong, L.; Fan, K.; Cui, L.; Lu, F.; Liu, P.; Li, B.; Feng, S.; Wang, L. Constructing  $Fe-N_4$  Sites through Anion Exchange-Mediated Transformation of Fe Coordination Environments in Hierarchical Carbon Support for Efficient Oxygen Reduction. *Angew. Chem., Int. Ed.* **2023**, *135* (38), No. e202309784.
- (40) Wu, D.; Wu, S.; Zhang, G.; Hui, C.; Cao, D.; Guo, S.; Feng, H.; Wang, Q.; Cheng, S.; Cui, P.; et al. Boosting  $Li-O_2$  Battery Performance via Coupling of P-N Site-Rich N, P Co-Doped Graphene-Like Carbon Nanosheets with Nano-CePO<sub>4</sub>. *Small* **2023**, *19* (19), No. 2206455.
- (41) Liu, Y.; Zong, L.; Zhang, Y.; Lu, F.; Wang, L. Joule Heating Synthesis for Single-Atomic Fe Sites on Porous Carbon Spheres and Armchair-Type Edge Defect Engineering Dominated Oxygen Reduction Reaction Performance. *Appl. Catal. B Environ. Energy* **2025**, *361*, No. 124673.
- (42) Chen, Y.; Li, Z.; Zhu, Y.; Sun, D.; Liu, X.; Xu, L.; Tang, Y. Atomic Fe Dispersed on N-Doped Carbon Hollow Nanospheres for High-Efficiency Electrocatalytic Oxygen Reduction. *Adv. Mater.* **2019**, *31* (8), No. 1806312.
- (43) Gong, X.; Zhu, J.; Li, J.; Gao, R.; Zhou, Q.; Zhang, Z.; Dou, H.; Zhao, L.; Sui, X.; Cai, J.; et al. Self-Templated Hierarchically Porous Carbon Nanorods Embedded with Atomic  $Fe-N_4$  Active Sites as Efficient Oxygen Reduction Electrocatalysts in Zn-Air Batteries. *Adv. Funct. Mater.* **2021**, *31* (8), No. 2008085.

- (44) Liu, J.; Wan, X.; Liu, S.; Liu, X.; Zheng, L.; Yu, R.; Shui, J. Hydrogen Passivation of M-N-C (M = Fe, Co) Catalysts for Storage Stability and ORR Activity Improvements. *Adv. Mater.* **2021**, *33* (38), No. 2103600.
- (45) Cheng, J.; Zhang, Z.; Shao, J.; Wang, T.; Li, R.; Zhang, W. Construction of an Axial Charge Transfer Channel between Single-Atom Fe Sites and Nitrogen-Doped Carbon Supports for Boosting Oxygen Reduction. *Small* **2024**, *20* (40), No. 2402583.
- (46) Chen, M.; Ma, J.; Feng, Y.; Wu, Y.; Hu, G.; Liu, X. Advanced Characterization Enables a New Era of Efficient Carbon Dots Electrocatalytic Reduction. *Coord. Chem. Rev.* **2025**, *535*, No. 216612.
- (47) Chen, M.; Ma, J.; Chen, X.; Liu, Q.; Feng, Y.; Liu, X. Support Engineering of Single-Atom Electrocatalysis: Mechanism Analysis and Application Expansion. *Chin. Chem. Lett.* **2025**, No. 111637.
- (48) Malko, D.; Kucernak, A.; Lopes, T. In Situ Electrochemical Quantification of Active Sites in Fe-N/C Non-Precious Metal Catalysts. *Nat. Commun.* **2016**, *7* (1), No. 13285.
- (49) Chu, Y.; Luo, E.; Wei, Y.; Zhu, S.; Wang, X.; Yang, L.; Gao, N.; Wang, Y.; Jiang, Z.; Liu, C.; et al. Dual Single-Atom Catalyst Design to Build Robust Oxygen Reduction Electrode via Free Radical Scavenging. *Chem. Catal.* **2023**, *3* (3), No. 100532.
- (50) Liu, C.; Shi, W.; Yuan, Y.; Zhu, K.; Zhang, Q.; Li, S.; Yang, X.; Bai, Z.; Yang, L. Cascade Hydrogen Peroxide Reduction Reaction Endows Cu-Fe Dual-Atom Catalyst with Durable Oxygen Reduction Performance. *Adv. Funct. Mater.* **2025**, *35* (35), No. 2503079.
- (51) Kim, K.; Kim, G.; Jeong, T.; Lee, W.; Yang, Y.; Kim, B.-H.; Kim, B.; Lee, B.; Kang, J.; Kim, M. Activating the Mn Single Atomic Center for an Efficient Actual Active Site of the Oxygen Reduction Reaction by Spin-State Regulation. *J. Am. Chem. Soc.* **2024**, *146* (49), 34033–34042.
- (52) Zhang, P.; Chen, H.-C.; Zhu, H.; Chen, K.; Li, T.; Zhao, Y.; Li, J.; Hu, R.; Huang, S.; Zhu, W.; et al. Inter-Site Structural Heterogeneity Induction of Single Atom Fe Catalysts for Robust Oxygen Reduction. *Nat. Commun.* **2024**, *15* (1), 2062.
- (53) Hu, Y.; Niu, S.; Zhang, Z.; Chao, T.; Zhao, T.; Yu, G.; Zhou, F.; Liang, X.; Jin, H.; Yang, Z.; et al. Axial Chlorine Engineering of p-Block Antimony Atomic Sites Boosts Oxygen Reduction. *J. Am. Chem. Soc.* **2025**, *147* (24), 21231–21240.
- (54) Yang, N.; Zheng, X.; Li, L.; Li, J.; Wei, Z. Influence of Phosphorus Configuration on Electronic Structure and Oxygen Reduction Reactions of Phosphorus-Doped Graphene. *J. Phys. Chem. C* **2017**, *121* (35), 19321–19328.
- (55) Singh, K. P.; Bae, E. J.; Yu, J.-S. Fe-P: A New Class of Electroactive Catalyst for Oxygen Reduction Reaction. *J. Am. Chem. Soc.* **2015**, *137* (9), 3165–3168.
- (56) Zang, Y.; Liu, Y.; Lu, R.; Yang, Q.; Wang, B.; Zhang, M.; Mao, Y.; Wang, Z.; Lum, Y. Tuning Transition Metal 3d Spin State on Single-Atom Catalysts for Selective Electrochemical CO<sub>2</sub> Reduction. *Adv. Mater.* **2025**, *37* (16), No. 2417034.
- (57) Hammer, B.; Norskov, J. K. Why Gold is the Noblest of all the Metals. *Nature* **1995**, *376*, 238–240.
- (58) Zong, L.; Li, M.; Li, P.; Fan, K.; Wang, L. Rigid Ligand Confined Synthesis of Carbon Supported Dimeric Fe Sites with High-Performance Oxygen Reduction Reaction Activity for Quasi-Solid-State Rechargeable Zn-Air Batteries. *Angew. Chem., Int. Ed.* **2025**, *64* (1), No. e202413933.
- (59) Wang, Q.; Feng, Q.; Lei, Y.; Tang, S.; Xu, L.; Xiong, Y.; Fang, G.; Wang, Y.; Yang, P.; Liu, J.; et al. Quasi-Solid-State Zn-Air Batteries with an Atomically Dispersed Cobalt Electrocatalyst and Organohydrogel Electrolyte. *Nat. Commun.* **2022**, *13* (1), 3689.



CAS BIOFINDER DISCOVERY PLATFORM™

## CAS BIOFINDER HELPS YOU FIND YOUR NEXT BREAKTHROUGH FASTER

Navigate pathways, targets, and diseases with precision

Explore CAS BioFinder

